Chapter 4

# Thin Film Solar Cells: Modeling, Obtaining and Applications

P.P. Horley, L. Licea Jiménez, S.A. Pérez García,
J. Álvarez Quintana, Yu.V. Vorobiev, R. Ramírez Bon,
V.P. Makhniy and J. González Hernández

Additional information is available at the end of the chapter

http://dx.doi.org/10.5772/54058

## 1. Introduction

The development of human civilization was fueled by different energy sources throughout its history, with the past decades clearly showing a trend of using environment-friendly energy. Among the energy sources available from the Nature, solar energy has a special place [1, 2]. It is available in vast quantities, especially in countries with high insolation level such as México. Transformation of solar light into electricity takes place in photovoltaic devices – solar cells – that do not require much maintenance throughout their operation cycle and can function as stand-alone devices allowing the use of electrical equipment even in most remote areas. The energy produced by the solar cells during the day can be stored in accumulators and used during the night, making solar-powered equipment practically self-sustainable if the required number of sunlight hours per day is available.

Currently, most commercial solar cells are made of silicon due to its vast availability and silicon technology that reached the state of perfection, allowing to achieve the conversion efficiency of almost 28% (single silicon cell, [3]). Actually, world production of photovoltaics is dominated by polycrystalline silicon cells representing 94% of the market [4]. These devices based on silicon wafers are called the "first generation" of photovoltaic technology. Monocrystalline silicon devices are effective but expensive. Similarly, solar cells based on other semiconductor materials, called "second generation", such as group II-VI and III-V heterostructures, are capable of efficiencies over 40% (GaInP/GaAs/GaInNAs, [3]) but depend significantly on the quality of the junction that may contain defects acting as effective recombination centers, reducing considerably the concentration of photo-generated carriers.

Finally, there is the "third generation" of photovoltaic devices that embraces solar cells based on organic semiconductors. These materials usually afford moderate efficiency – about 11% (dye-sensitized cells [3]); however, they are cheap and easy to obtain, which is a very attractive point for industrial-scale production. Also, organic materials can be deposited on flexible substrates, widening the spectrum of their possible applications.

In this chapter, we present the results for several types of heterojunction solar cells that are particularly focused on the use of thin film devices for photovoltaic conversion [5]. We discuss the benefits of computer simulations for improvement of AlGaAs/GaAs solar cells, suggesting the optimal values of aluminum contents and thickness of the window layer. We propose the isovalent substitution method as a promising technological approach for crafting near-to-perfect junction boundary with reduced mismatch of lattice parameters and thermal expansion coefficients, illustrating it for the case of CdTe/CdS heterostructures. Aiming to lower the cost of solar cell production, we consider the option of chemical bath deposition for CdS/PbS solar cell, proposing environment-friendly variation that significantly reduces (and even disposes of) the use of toxic ammonia that is characteristic for a common chemical bath deposition process for CdS films. We also address the question of organic solar cells, discussing the mechanisms of current transport in a cell based on poly (3-hexylthiophene). Finally, we consider the question of excess heating that is characteristic to the photovoltaic devices (especially those operating under concentrated light conditions), proposing to use the experience gained from nano-thermoelectric formations used to remove the extra heat from the devices composing microchips.

## 2. General theoretical modeling

Let us consider the basic physical processes taking place in a semiconductor solar cell with a heterojunction (Fig. 1). The device is composed by two semiconductors with different band gap values [1, 6]. The wider-band material forms so-called window layer (for which the corresponding characteristics in Fig. 1 have the subscript “W”) and is used to process high-energy photons, allowing low-energy photons to pass through. These became absorbed in the narrower-band material forming the absorber layer (hence the subscript “A” in Fig. 1). The thickness of the corresponding layers will be referred to as $D_W$ and $D_A$, correspondingly, making the total device thickness equal to $D_{WA} = D_W + D_A$. The presence of window and absorber layers allows to optimize solar spectrum use and reduce device heating that is more prominent in p-n junctions, where more absorbed photons have the energies exceeding band gap of the material. The other benefit consists in increase of material choice for creating the junction, because not all semiconductors can be obtained in both modifications with p- and n- conductivity. On the negative side, the mismatch of lattice parameters of junction components create undesirable defects, and difference in thermal expansion coefficient may be critical for stability of the device if used under the elevated temperatures.

The contact of two materials with different conductivity type leads to the formation of space charge region [7] associated with diffusion potential difference $U_d$. Within this so-

http://dx.doi.org/10.5772/54058

called depletion region of width $w_n + w_p$ (Fig. 1) energy band bending occurs. In general case, due to the difference of band gap values of window and absorber layers ($E_{gW}$ and $E_{gA}$, respectively) there will be band discontinuities $\Delta E_V$ and $\Delta E_C$, introducing additional energy barriers for the carriers and paving the way for different types of tunneling effects. The band diagram of a heterojunction can be constructed using electron affinities for both materials – $\chi_W$ and $\chi_A$, respectively, which allows to construct band diagram of the structure.

Under illumination, the electrons obtain the energy sufficient for moving into conduction band, creating holes in the valence band. The resulting non-equilibrium electron-hole pair can disappear due to recombination. However, if it is generated in the vicinity of the junction, the embedded electric field of the space charge region will exert different forces on the carriers in accordance with their charges, moving them towards the contacts where they contribute to the photo-current of the external circuit.

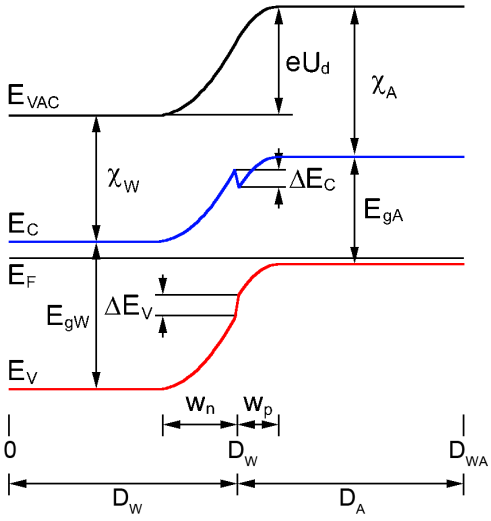


**Figure 1.** Band diagram of a heterojunction with main parameters denoted.

The transport of the carriers, in addition to the action of the embedded electric field, is also governed by the diffusion caused by the difference in concentrations of electrons and holes in the corresponding parts of the device. This mechanism can be described as [8]

$$J_n = en(x)\mu_n E(x) + eD_n \frac{dn}{dx} \tag{1}$$

$$J_p = ep(x)\mu_p E(x) - eD_p \frac{dp}{dx} \tag{2}$$

where $n$, $p$ are concentration of electrons and holes, $\mu_n$ and $\mu_p$ are their mobilities and $D_n$, $D_p$ are diffusion coefficients. The action of the electric field is limited to the space charge region that is characterized by the thickness

$$w_n + w_p = \sqrt{\frac{2\varepsilon_W \varepsilon_A N_A (U_d - U)}{eN_D(\varepsilon_W N_D + \varepsilon_A N_A)}} + \sqrt{\frac{2\varepsilon_W \varepsilon_A N_D (U_d - U)}{eN_A(\varepsilon_W N_D + \varepsilon_A N_A)}} \tag{3}$$

with dielectric constants of window and absorber materials $\varepsilon_W$ and $\varepsilon_A$, respectively. The values of $N_D$ and $N_A$ correspond to the concentration of donors and acceptors that define conductivity type of the materials forming heterojunction. The height of the energy barrier, $U_d$, can be manipulated by application of a voltage $U$, which is also included into (3). Calculating the value of $w_n + w_p$ it can be shown that the space charge region usually is of negligible thickness in comparison with that of the entire device. Therefore, one can simplify the equations (1) and (2) by keeping only diffusion terms:

$$\begin{aligned} J_n &= eD_n \frac{dn}{dx} \\ J_p &= -eD_p \frac{dp}{dx} \end{aligned} \tag{4}$$

The resulting expressions can be rewritten relating current variation to the difference of recombination and generation rates. For simplicity, we will present here only equations describing window layer, for which the minority carriers are holes:

$$D_p \frac{d^2 p}{dx^2} = r_p - g_W \tag{5}$$

Recombination rate $r_p = \left(p - p_{n_0}\right)/\tau_{pW}$ depends on the difference between non-equilibrium and equilibrium concentrations of holes given in numerator, and a characteristic time $\tau_{pW}$ defined by recombination processes taking place in the system. Generation rate $g_W = \alpha_W \Phi_0 \exp(-\alpha_W x)$ includes absorption coefficient of the material $\alpha_W$, spectral power of incident light flux $\Phi_0$ and distance from the surface $x$. Substituting these expressions into formula (5) one will obtain

$$\frac{d^2 p}{dx^2} = \frac{p - p_{n0}}{L_p^2} - \frac{\Phi_0 \alpha_W}{D_p} e^{-\alpha_W x} \tag{6}$$

where $L_p = \sqrt{D_p \tau_p}$ is the diffusion length for the holes. Equation (6) should be solved taking into account the boundary conditions. On the front of the cell, the variation of hole concentration is connected with surface recombination rate $s_p$:

http://dx.doi.org/10.5772/54058

$$\left.\frac{dp}{dx}\right|_{x=0} = \frac{s_p}{D_p}(p(0) - p_{n0}) \tag{7}$$

At the boundary with space charge region, the concentration of holes is equal to:

$$p(D_W - w_n) = p_{n0} exp\left(eU / k_B T\right) \tag{8}$$

where $k_B T$ is a product of the Boltzmann constant and the temperature. The solution of the equation (6) is usually written in the form

$$p(x) = p_{n0} + C_0^p e^{-\alpha_W x} + A_p e^{x/L_p} + B_p e^{-x/L_p} \tag{9}$$

with $C_0^p = \frac{\alpha_W \Phi_0 L_p^2}{D_p(1-\alpha_W^2 L_p^2)}$ and coefficients $A_p$ and $B_p$ that can be found from boundary conditions. The similar equations can be obtained for electrons as minority carrier in absorber part of the device, yielding the general solution for carrier concentration as

$$n(x) = n_{p0} + C_0^n e^{-\alpha_W (x - D_W)} + A_n e^{x/L_n} + B_n e^{-x/L_n} \tag{10}$$

where $D_W$ appearing in the first exponent denotes the decrease of light flux upon passing through the window layer. Now, the total current through passing to the external circuit can be obtained as the sum of electron and hole currents at the contacts together with total photo-generation current reduced by integral describing recombination losses:

$$J = J_p(0) + J_n(D_{WA}) + e\int_0^{D_{WA}} g(x)dx - e\int_0^{D_{WA}} r(x)dx. \tag{11}$$

Two first terms in (11) can be easily found using the expressions for carrier concentrations (9), (10) and their relation to the corresponding current components (4):

$$J_p(0) = eD_p\left[\alpha_W C_0^p + \frac{1}{L_p}\left(B_p - A_p\right)\right] \tag{12}$$

$$J_n(D_{WA}) = -eD_n\left[\alpha_A C_0^n e^{-\alpha_A D_A} + \frac{1}{L_n}\left(B_n e^{-D_{WA}/L_n} - A_n e^{D_{WA}/L_n}\right)\right] \tag{13}$$

The generation term from (11) can be calculated analytically:

$$e\int_0^{D_{WA}} g(x)dx = \Phi_0\alpha_W e\int_0^{D_W} e^{-\alpha_W x}dx + \alpha_A\Phi_0 e^{-\alpha_W D_W} e\int_0^{D_A} e^{-\alpha_W (x-D_W)}dx$$
$$= \Phi_0 e\left[1 - e^{-(\alpha_W D_W + \alpha_A D_A)}\right] \tag{14}$$

The recombination term is calculated numerically, taking into account the distribution of non-equilibrium carrier concentration in window/absorber and various recombination mechanisms such as direct recombination, Hall-Shockley-Read recombination involving impurity levels in band gap, and Auger recombination for high-energy carriers that transfer their excess energy to another particle [8].

For numerical simulations we considered the heterojunction $Al_xGa_{1-x}As/GaAs$ [9] characterized by a small lattice mismatch of 0.127%. The window layer remains direct-band semiconductor for aluminium contents less than 45%. Material parameters used in our simulations are listed in Table 1 as functions of aluminium content $x$ and temperature $T$.

| Parameter | Value or calculation formula |
|---|---|
| Dielectric constant $\varepsilon$ | $12.90 - 2.84x$ |
| Electronic affinity $\chi$, eV | $4.07 - 1.1x$ |
| DOS effective masses | $m_n^* = (0.067 + 0.083x)\, m_0$; $m_p^* = (0.62 + 0.14x)\, m_0$ |
| Electron mobility $\mu_n$, $cm^2/(Vs)$ | $(8 - 22x + 10x^2)\cdot 10^3$ |
| Hole mobility $\mu_p$, $cm^2/(Vs)$ | $(3.7 - 9.7x + 7.4x^2)\cdot 10^2$ |
| Band gap $E_g$, eV | $1.424 + 1.247x - (5.4\cdot 10^{-4}T^2)/(T+204[K])$ |

**Table 1.** Parameters of $Al_xGa_{1-x}As$ used in calculations

In the framework of the current chapter, we studied the dependence of window layer thickness $D_W$ on the efficiency of AlGaAs/GaAs solar cell. All calculations were done for AM1.5 illumination [10]. First, we considered the question about the thickness ratio of window/absorber layers (Fig. 2). The resulting plot has roughly triangular shape with the grayed out area in the bottom left corner where the system is not converging to any solution. As one can see from the figure, the efficiency $\eta$ exceeding 24% is obtained for thicker cell ($D_{WA}$ = 300 μm), which is expected because the junction should have enough material for a considerable absorption of solar light. When the cell is 3 μm thick, the value of $\eta$ reaches 20% at most. It is also clear from the figure that the cell performs better with a thin window layer. For example, the efficiency over 20% is reachable for a thick cell with window layer thickness under 0.5% of $D_{WA}$, i.e., $D_W < 1.5$ μm. This result proves that the embedded electric field of space

charge region should be located quite close to the surface where the major photo-generation of non-equilibrium carriers takes place, ensuring efficient separation of electron-hole pairs and reducing losses due to the recombination processes. If the junction is located deeper into the cell, the embedded field becomes less efficient. Also, thicker absorber layer augments the number of processed photons that increases the current flowing to the external circuit.

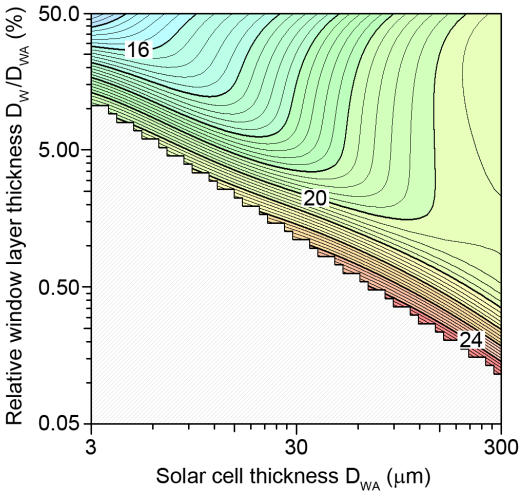


**Figure 2.** Dependence of $Al_{0.29}Ga_{0.71}As/GaAs$ solar cell performance as a function of window and cell thickness

Another important point is the adjustment of band gap difference between the heterojunction components that modifies the percentage of light processed by window and absorber layers. Having in mind that thicker cell has better overall performance, we performed calculations varying the aluminum contents $x$ in $Al_xGa_{1-x}As$ and thickness of the window layer. These results are presented in Fig. 3. Similarly to Fig. 2, the case of ultrathin window precludes numerical convergence and is greyed out. As one can see from the figure, the efficiency landscape has two prominent details. For comparative thick window layer with $D_W$ above a micron, it has a pronounced maximum at $x = 29.5\%$that does not shift with variation of $D_W$ by two orders of magnitude. The maximum changes into a wide plateau with $\eta > 17\%$ for $x$ exceeding 20%, following with a quick drop of efficiency for decreasing aluminum content. Increase of $x$ above 30% also causes abrupt drop of the efficiency. We explain this behavior by optimal adjustment of band gaps $E_{gW}$ and $E_{gA}$ ensuring good separation of solar spectra into "high" and "low"-energy parts processed by window and absorber layer, respectively, for $20\% < x < 30\%$. For lower $x$, the difference of band gaps is insufficient. For higher $x$, the difference is too big so that the energy of the photons passing the window layer is high in comparison with $E_{gA}$, which will result in excess Auger recombination rate and increased cell heating.

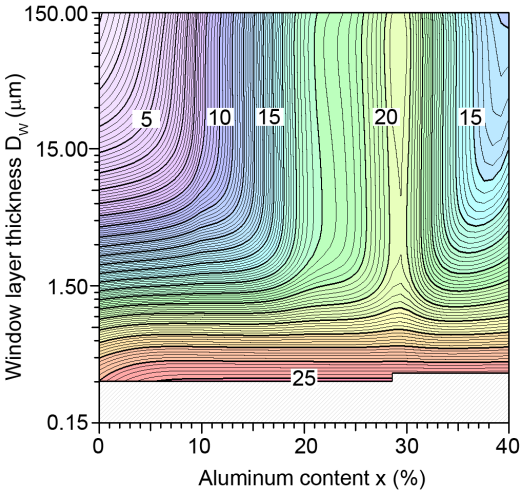


**Figure 3.** Efficiency of $Al_xGa_{1-x}As/GaAs$ solar cell as a function of window layer thickness $D_W$ and aluminum contents $x$

However, when window layer becomes very thin ($D_W$ < 1μm), the system starts to behave differently. Now, the generation of the carriers in direct vicinity of junction boundary provides a significant benefit by quick and efficient separation of carriers by electric field associated with space charge region, reducing recombination losses. Nevertheless, even the contour line for $\eta$ = 23% shows that the cell performs slightly better when aluminum contents gravitates towards $x$ = 30%.

Therefore, theoretical treatment of semiconductor solar cell followed by numerical simulations allowed to obtain useful information about the system, which can significantly simplify the experimental optimization of solar cell parameters by suggesting the most promising ranges of parameters that corresponds to the highest efficiency of photovoltaic conversion of solar energy.

## 3. Solar cells with CdTe layers grown by isovalent substitution

Among the materials used for solid-state cells, cadmium telluride occupies a special place due to its near-optimal band width of 1.5 eV at 300 K. Direct band of CdTe favors manufacture of thin-film barrier structures [5, 6]. However, despite it is possible to grow CdTe with n- and p-conductivity, the p-n junction solar cells of cadmium telluride are impractical due to high absorption and recombination. Schottky barriers are also not quite useful because many metals form comparatively low barriers with p- and n-type cadmium telluride [11]. Under these conditions, the major flexibility in device design can be attained for heterojunctions, among which the most prominent are thin-film structures of p-CdTe/n-CdS. It is quite easy to obtain solar cells with efficiency of $\eta \approx 16\%$, but much device optimization work is

http://dx.doi.org/10.5772/54058

required to achieve the theoretical performance limit of 28% [6]. One of the main reasons reducing the efficiency of solar cell is a large concentration of defects $N_S$ at the junction boundary caused by a mismatch of crystalline and thermal parameters of device components [12]. Therefore, it is important to search for the best material especially for wide-band window layer and improve the reproducibility of technology aiming to create heterostructures with a perfect junction boundary.

One of the promising approaches to solve this problem involves the method of isovalent substitution (IVS) [13], offering considerable advantages over the traditional methods of heterojunction manufacturing [5, 12]. The substituted heterolayers grows down into the substrate, which defines and stabilizes the crystalline structure of the layer. Thus, IVS is used to obtain stable layers of materials with crystalline modifications that do not exist in bulk form. The layers of intermediate solid solutions relax the difference of lattice parameters and thermal expansion coefficients, ensuring low Defect concentration at the junction boundary. Finally, residual base substrate atoms act as isovalent impurities, significantly increasing the temperature and radiation stability of the material [14]. This section reports successful use of isovalent substitution method for formation of heterojunctions of CdTe with wide-band II-VI compounds such as CdS, ZnTe and ZnSe.

The base substrates with the size of 4×4×1 $mm^3$ were cut from bulk CdS, ZnTe and ZnSe crystals grown by Bridgman method from the stoichiometric melt. At the room temperature the substrates of CdS and ZnSe had n-type conductivity; ZnTe samples were of p-type due to presence of intrinsic point defects. After mechanical polishing the plates were etched chemically in the solution of $Cr_2O_3$ : HCl = 2 : 3, rinsed in distilled water and dried. These operations ensured mirror-reflective surface of the substrates and bulk luminescence within the corresponding spectral ranges. The heterostructures were formed by annealing of the substrates in quartz containers pumped out to $10^{-4}$ Torr at the temperatures of $T_A$=800 –1000 K. The additional charges loaded into containers are listed in Table 2.

| **Substrate** | n-CdS | p-ZnTe | n-ZnSe |
|---|---|---|---|
| **Charge** | Charge of CdTe, Te and $LiCO_3$ salt | Charge of CdTe and Cd | Charge of CdTe |

**Table 2.** Loads to the containers required to form heterostructures of corresponding type

Annealing process leads to formation of cadmium telluride layer on top of the base substrates, which was verified by spectra of optical reflectivity and transmittivity. The thickness of CdTe layers is controlled by deposition conditions and film conductivity type results to be opposite to that of the substrate. To make diode structures, we polished off the CdTe layer from one side down to the substrate. Ohmic contacts were deposited by melting in In for n-type material and vacuum-sputtering of Ni for the p-type one. The sketch of resulting p-CdTe/n-CdS structure is given in the inset to Fig. 4.

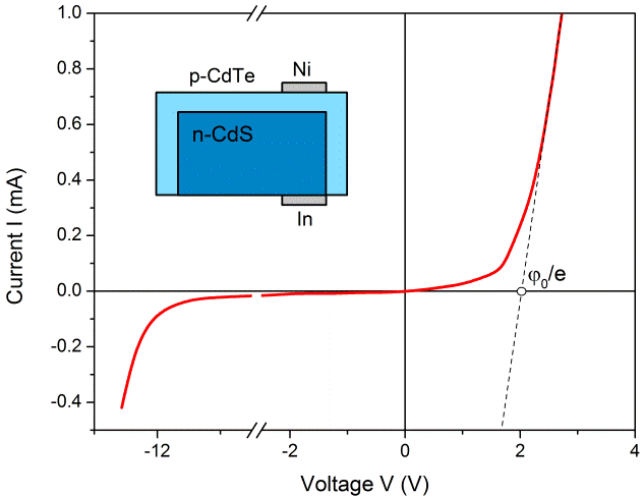


**Figure 4.** Typical CVC of p-CdTe/n-CdS heterojunction at 300 K. The inset shows a schematic view of the structure.

The heterojunctions studied featured pronounced diode characteristics with rectification coefficient above $10^4$ at 300 K and voltage of 1 V. The typical dark current-voltage curve (CVC) of an example p-CdTe/n-CdS heterojunction is given in Fig. 4. The potential barrier height $\varphi_0$ can be estimated extrapolating the straight branch of the curve towards the intersection with the voltage axis (Fig. 4). The value of $\varphi_0$ depends on heterojunction type and technological condition used to obtain it, with the maximum barrier values listed in Table 3.

| Heterojunction | p-CdTe/n-CdS | n-CdTe/p-ZnTe | p-CdTe/n-ZnSe |
|---|---|---|---|
| $\varphi_0$, eV | 1.25 | 1.4 | 1.3 |
| $V_{OC}$, V | 0.6 | 0.8 | 0.7 |

**Table 3.** Maximum barrier height and open circuit voltage of heterojunctions at 300 K

Our analysis shows that current-voltage curves at lower bias obey the expression that corresponds to dominating carrier recombination in the space charge region [6]

$$I_{gr} \approx I_{gr}^{0} \exp(eV / 2kT) \tag{15}$$

with intercept current $I_{gr}^{0}$ obtained for $V$=0. Energy slope of $I_{gr}^{0}(T)$ curve plotted in axis frame $\ln\left(I_{gr}^{0} - 1/T\right)$ is about 1.6-1.7 eV, which agrees with the bandgap of cadmium telluride at 0 K, proving that the space charge region is mainly localized in CdTe and recombination takes part in the thinner component of the junction. Under the higher bias the formula (1) transforms into less steep dependence [5]

$$I_{grt} \approx I_{grt}^{0} \exp(\alpha \mathrm{V} + \beta \mathrm{T}) \tag{16}$$

where $I_{grt}^{0}$ is the intercept current and parameters $\alpha = (5-15)\ V^{-1}$, $\beta = (0.01-0.02)\ K^{-1}$ are independent on both voltage and temperature. For the bias approaching $\varphi_0/e$, current transport in the device becomes dominated by over-barrier current $I_d$, which for the heterojunctions p-CdTe/n-CdS and p-CdTe/n-ZnSe is provided by electrons and for n-CdTe/p-ZnTe diodes – by holes. The inverse current in obtained heterojunctions is determined by carrier tunneling (low bias case) and avalanche processes (high bias case).

The current voltage curve of illuminated structures for $eV \geq 3kT$ obeys expression

$$I_{SC} = I_{SC}^{0} \exp(eV_{OC} / 2kT) \tag{17}$$

with short circuit current $I_{SC}$ and open circuit voltage $V_{OC}$. The presence of two in denominator of the exponent corresponds to the major carrier generation in the space charge region. Thermal dependence of the intercept $I_{SC}^{0}$ photocurrent value is determined mainly by the exponential coefficient $\exp(-E_g/2kT)$. The band gap value $E_g$ appearing here characterizes the material in which the most intensive generation takes place. In the heterostructures synthesized under low $T_A$ the value of $E_g$ is about 1.6 eV, which correspond to the band gap of CdTe at 0 K. At higher synthesis temperature $E_g$ increases up to 1.8-2.0 eV, suggesting that photogeneration of the carriers takes place in solid solution layers at the junction boundary. Dependence of short circuit current on the illumination intensity $L$ remains linear even if the latter varies by five orders of magnitude. The open circuit voltage changes proportionally to $\ln L$ for low light, tending to saturation under high illumination intensity. Using 100 W tungsten lamp as a power source, we were able to measure $V_{OC}$ values at 300 K (see Table 3).

In contrast to the above-discussed integral device characteristics, the spectral data are more variable by depending significantly on heterojunction type and technological conditions during its formation. It is worth noting general features of photosensitivity spectra $S$, in particular, the fact that $S$ curves are limited by photon energies corresponding to band gap values of heterojucntion components (Fig. 5). The shape of the spectrum and position of its peaks is again defined by the part of the device with major generation of photo-carriers.

Let us analyze this question in detail for a particular case of p-CdTe/n-CdS heterostructure. As one can see from Figure 6, the photosensitivity of a junction synthesized at $T_A$ = 800 – 1000 K embraces a wide interval of photon energies and has a blurred peak. This is caused by the presence of the solid solution layer of $CdS_xTe_{1-x}$ responsible for smooth variation of $E_g$ in the area of generation and separation of non-equilibrium carriers.

High-energy edge ends at $h\nu \approx 2.5$ eV, which is close to the $E_g$ of cadmium sulfide. Photons with $h\nu > 2.5$ eV are absorbed in CdS deeper than diffusion length of the minority carriers and thus become lost due to recombination processes. The spectral sensitivity below the band gap of cadmium telluride is caused by non-linearity of band gap dependence for solid

solutions $CdS_xTe_{1-x}$ on composition x, which is known [14] to have a minimum at $E_g \approx 1.2$ eV for $x \approx 0.2$; the photons absorbed in this layer will contribute to sensitivity with $h\nu < 1.5$ eV.

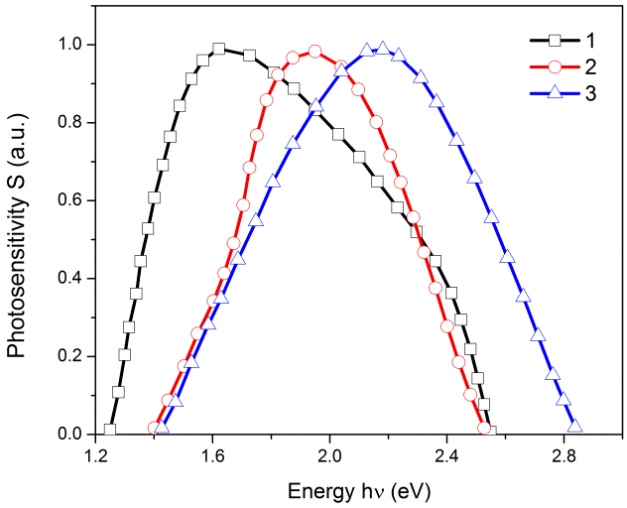


**Figure 5.** Typical photosensitivity spectra of heterojunctions: 1) p-CdTe/n-CdS, 2) n-CdTe/p-ZnTe and 3) p-CdTe/n-ZnSe at 300 K and illumination from wide-band component side

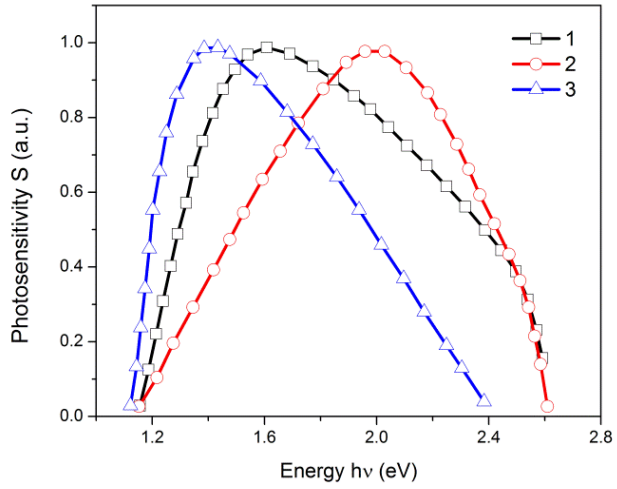


**Figure 6.** Normalized photosensitivity spectra of p-CdTe/n-CdS heterojunction formed under different temperatures: 1) 800 K, 2) 900 K, and 3) 1000 K

http://dx.doi.org/10.5772/54058

We measured main parameters of heterojunctions related to their possible photovoltaic applications. All measurements were done under AM2 illumination at 300 K and are listed in Table 4. The density of short circuit current was calculated from the experimental $I_{SC}$, accounting for the effective area of the diodes that is about 0.1 cm$^2$.

| Heterostructure | $I_{SC}$, mA/cm$^2$ | $V_{OC}$, V | $\eta$, % | *FF* |
|---|---|---|---|---|
| p-CdTe/n-CdS | 18 | 0.5 | 10 | 0.7 |
| n-CdTe/p-ZnTe | 10 | 0.7 | 5 | 0.5 |
| p-CdTe/n-ZnSe | 11 | 0.6 | 6 | 0.55 |

**Table 4.** Main parameters of solar cells based on heterostructures studied

As one can see from the table, the largest efficiency of 10% corresponds to the photovoltaic device based on p-CdTe/n-CdS, which is below the theoretical limit of 28% due to several reasons. Low fill-factor values *FF* are caused by a considerable series resistance of dozens of Ohms. This problem can be amended by low-resistance substrates and optimization of ohmic contacts primarily to the thin film layers of cadmium telluride. The benefits of obtained heterojunctions in first place is the low value of thermal efficiency variation $d\eta/dT$ = (0.02-0.03)%/K – that is, four times smaller than that of the silicon solar cells. This is important for solar concentrator applications, when the structure intensively heats. Thus, in spite of modest $\eta$, our heterojunctions may compete with GaAlAs ones, because for the same $d\eta/dT$ they are significantly cheaper and simpler in manufacture. It is also worth mentioning that the presence of isovalent impurities in CdTe heterolayers increments radiation stability of the material, which is especially important for open space applications.

## 4. Heterojunction CdS/PbS cells obtained by chemical bath deposition

Continuing the discussion of solid state solar cells, let us perform optimization of absorber layer keeping the window layer of wide-band CdS, paying a special attention to simplification of deposition technology with an aim to reduce the production costs. Among the main techniques used for the deposition of CdS thin films, we highlight chemical bath deposition (CBD) that produces layers with excellent characteristics because of their compactness and uniformity due to congruent growth and high relative photoconductivity [16, 17]. Furthermore, CBD is a good method for a large area deposition, which is convenient for solar cell fabrication on industrial scale. In CBD technique, the properties of thin films can be controlled by several parameters such as pH of the reaction solution, concentration of the chemical precursors, temperature, deposition time, etc. However, on the other hand, the CBD technique for the deposition of CdS films has serious drawbacks such as large amount of Cd-containing toxic waste produced in the process. Moreover, the classic CBD uses highly volatile and harmful ammonia as the complexing agent in the reaction solution, which can become even more critical in large scale production. These disadvantages catalyze intensive research

aiming to improve the CBD process. For example, ammonia has been substituted with more convenient complexing agents such as ethylendiamine, ethanolamine, triethanolamine, nitrilotriacetic acid and sodium citrate. In particularly, we have developed CBD process based on sodium citrate in place of ammonia [17].

Sodium citrate is a cheap and practically harmless organic compound widely employed in food industry as flavoring or preservative, also as a common ingredient for drinks. We reported main characteristics of CdS films deposited over glass substrates by the partial and complete substitution of ammonia by sodium citrate in the CBD process, resulting in thin films of high crystallinity degree, homogeneity and compactness that performed pretty well as window layers in CdS /CdTe thin film solar cells and as active layers in field effect thin film transistors. Here we would like to discuss CdS window layers obtained by ammonia-free CBD process for CdS/CdTe and CdS/PbS solar cell heterostructures.

The CdS/CdTe and CdS/PbS solar cells were deposited in superstrate geometry onto ITO-coated glass substrates employing two types of chemically-deposited CdS window layers labeled X-CdS and Y-CdS, respectively [18]. The CBD process for Y-CdS films is ammonia-free sodium citrate-based process, consisted in a 100 ml reaction solution prepared in a beaker by the sequential addition of 10 ml of 0.05 M cadmium chloride $CdCl_2$, 20 ml of 0.5 M sodium citrate $Na_3C_6H_5O_7$, 5 ml of 0.3 M potassium hydroxide KOH, 5 ml of a pH 10 borate buffer, 10 ml of 0.5 M thiourea $CS(NH_2)_2$ and deionized water to complete the total volume. The deposition process for X-CdS films consisted in the reaction solution including 25 ml of 0.1 M $CdCl_2$, 20 ml of 1 M $Na_3C_6H_5O_7$, 15 ml of 4 M ammonium hydroxide $NH_4OH$, 10 ml of 1 M $CS(NH_2)_2$ and deionized water to complete the total volume of 100 ml. In this case, the complexing agent is the mixture of ammonium hydroxide and sodium citrate. In both processes, the beaker with the reaction solution was placed in a thermal water bath at 70 °C. The deposition time was adjusted (20-60 min) to obtain CdS window layers some 100 nm thick. The deposition rates depend on the concentration of the precursors in the reaction solution. It was noticed that the amount of Cd ions is much higher in deposition of X-CdS films – 2.81 mg/ml; for Cd-Y films the numbers are lower – 0.56 mg/ml.

The CdTe thin films on ITO/CdS substrates were deposited by the close-spaced vapor transport-hot wall (CSVT-HW) technique using CdTe powders of 99.99% purity. The deposition of CdTe was performed in $Ar/O_2$ atmosphere, with each components having partial pressure of 0.05 Torr. The temperatures of the substrate and the source were set to 550 °C and 650 °C, respectively. The deposition process was carried out for 4 minutes. Under these conditions, the resulting thickness of the CdTe layers was approximately 3 μm. After deposition, the CdTe thin films were coated with a 200 nm $CdCl_2$ layer and annealed at 400 °C for 30 min in the air. To create back contact, we deposited by evaporation two layers of Cu and Au with thickness of 20 Å and 350 nm, respectively. The area of the contacts on CdTe side was 0.08 $cm^2$; after the deposition, the device was annealed at 180 °C in argon atmosphere. The efficiency of CdS/CdTe solar cells was determined from current-voltage measurements under 50 $mW/cm^2$ illumination.

To produce PbS/CdS solar cells, we deposited PbS film over ITO/CdS substrates by the CBD process that included 2.5 ml of 0.5 M lead acetate, 2.5 ml of 2M NaOH, 3 ml of 1 M thiourea,

http://dx.doi.org/10.5772/54058

2 ml of 1 M triethanolamine and deionized water to bring the total volume to 100 ml. The films were deposited at 70°C for one hour and their thickness was about of 4.2 μm. The solar cell structures were completed with 0.16 $cm^2$ printed layer of conducting graphite on the PbS films, serving as back contact. The efficiency of the CdS/PbS solar cells was determined from CVC measurements under 90 $mW/cm^2$ illumination.

Figure 7 shows the CVC for the CdS/CdTe solar cells, with X-CdS and Y-CdS window layers. The corresponding performance parameters of both types of solar cells are presented in Table 5. It is observed that the performance of solar cells with X-CdS window layer is better, featuring short circuit current density of 11.9 $mA/cm^2$, open circuit voltage of 630 mV, fill factor of 58%, yielding the efficiency of 8.7%.

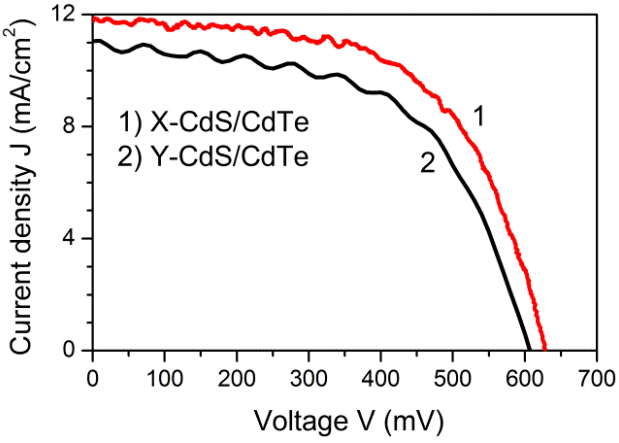


**Figure 7.** Current density versus voltage measurements under illumination of X-CdS/CdTe and Y-CdS/CdTe solar cells deposited on ITO conductive glass substrates.

Figure 8 presents the CVCs for X-CdS/PbS and Y-CdS/PbS solar cells. The performance parameters determined from these measurements are also given in Table 5. As expected, the performance of these solar cells is much lower because band gap of PbS is smaller, namely 0.4 eV. Nevertheless, the X-CdS window layer performs better also in these solar cells, allowing to reach short circuit current density of 14 $mA/cm^2$, open circuit voltage of 290 mV, fill factor of 36% and the efficiency of 1.63%. The low fill factor can be a consequence of high porosity characteristic for semiconductors obtained by the CBD method.

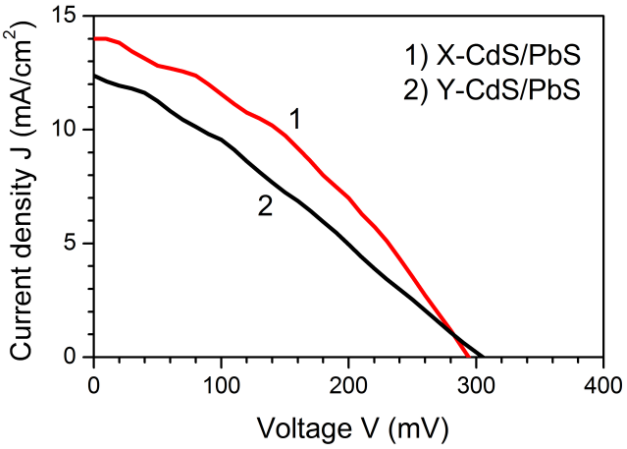


**Figure 8.** Current-voltage curves for illuminated X-CdS/PbS and Y-CdS/PbS solar cells deposited on ITO conductive glass substrates.

| Heterostructure | $V_{OC}$ (mV) | $J_{SC}$ (mA/cm$^2$) | *FF* (%) | $\eta$ (%) |
|---|---|---|---|---|
| X-CdS/CdTe | 630 | 11.9 | 58 | 8.7 |
| Y-CdS/CdTe | 607 | 11.1 | 56 | 7.5 |
| X-CdS/PbS | 290 | 14 | 36 | 1.63 |
| Y-CdS/PbS | 310 | 12.37 | 28 | 1.22 |

**Table 5.** Parameters of the X-CdS/CdTe and Y-CdS/PbS solar cells with two types of CdS window layers on ITO conductive glass substrates

The analysis of CdS/CdTe and CdS/PbS solar cells given above prove that both X-CdS and Y-CdS are appropriate materials for window layers, with higher efficiency achievable for the solar cells with the X-CdS window. The CBD process for CdS layers required to use both ammonia and sodium citrate as complexing agents. Nevertheless, this variation of CBD is more environmental-friendly with reduced ammonia use due to its partial substitution by sodium citrate. For Y-CdS layers, our optimized CBD process also reduces the amount of cadmium in the reacting solution by the factor of five comparing to the common process of CdS film deposition. Therefore, despite of lower efficiency of cells with Y-CdS window layers, completely ammonia-free process is more convenient for industrial-scale manufacture of CdS/CdTe and CdS/PbS solar cells.

http://dx.doi.org/10.5772/54058

## 5. Organic solar cells

The "third generation" of photovoltaic technology [19], appearing quite recently, divides into two principal approaches: achieving high efficiencies by creating multiple electron-hole pairs (including thermo-photonic cells) with high cost of the cell or, alternatively, to create very cheap cells with a moderate photovoltaic efficiency (~ 15-20%). Polymer solar cells have a significant impact potential for the second approach. A key point in the development of photovoltaic technology is reduction of cost for large scale production, which stimulates research for alternative materials (such as semiconductors, organics, polymers, heterostructures or composites) for solar cells and photovoltaic devices. The efficiency of inorganic solar cells reaches above 24% due to the use of expensive high purity materials. The production cost can be significantly reduced switching to cheaper constructions including nanocrystalline photoelectrochemical solar cells, pigment sensitivity (dye-sensitized cells), heterojunction polymer/fullerene organic-inorganic hybrid devices and solar cells based on inorganic nanoparticles. These solar cells are the classical example of an electronic device in which organic and inorganic materials complement each other in photovoltaic conversion. The nanomaterials and nanoparticles can also be used for development of energy saving and efficient electronic devices.

The semiconducting conjugated polymers are attractive for their use in photovoltaic cells, since they are strong absorbers and can be deposited onto flexible substrates at a low cost. Cells made from a conductive polymer and two electrodes tend to be inefficient because the photo-generated excitons (mobile excited states) are not separated by the electric field due to differences in the work functions of the electrodes; intensification of such separation helps to improve cell efficiency. Further performance boost can be achieved by optimization of cell design aiming to enhance charge transport and reduce recombination losses.

Polymer photovoltaic devices have a great potential, representing technological alternative to the classical solid-state renewable energy devices. The demand for low cost solar cells catalyzes new approaches and technological developments. In the past years, a significant scientific interest was attracted to solar cells based on organic molecules and conjugated polymers [20], which benefit much from mechanical flexibility and low weight. The polymers' band gap can be easily changed in organic synthesis, allowing production of polymers that absorb light at different wavelengths – which in the case of solid-state photovoltaics was achievable only by creating complicated tandem heterojunctions.

The main operation principles of organic photovoltaic cells differ from those taking place in solid-state semiconductor devices. In the organic material, light absorption leads to generation of excitons; in inorganic cells, illumination produces non-bound electrons and holes. To create photocurrent, it is necessary to separate the exciton into electron and hole before they recombine with each other. In a conjugated polymer, the stabilization of photo-excited electron-hole pairs can be achieved by polymer compounds containing acceptor molecules with electron affinity exceeding that of the polymer, but lower than the corresponding ionization potential. In addition, the highest occupied molecular orbital (HOMO) of the acceptor must have lower energy than those in the conjugated polymer. Under these conditions it becomes

energetically favorable for conjugated polymers to transfer photo-excited electrons to the acceptor molecule, keeping the hole at the lowest energy level corresponding to the valence band of the polymer.

Conjugated polymers have de-localized π-electron systems that can absorb sunlight, produce photo-generated charges and offer means for their transport. One of the promising materials from the family of conjugated polymers used for solar cell applications is the poly(3-hexylthiophene) P3HT [21, 22] with side chains that make it soluble in common organic solvents (Fig. 9), which allows material deposition by wet processing techniques such as spin coating (rotational coating), dip coating [23], ink jet printing [24, 25], screen printing and micromolding [26, 27]. All these methods can be performed at room temperature, normal atmospheric pressure and can be applied to the flexible substrates [28], paving an attractive route for mass-scale production of large-area solar cells at low cost.

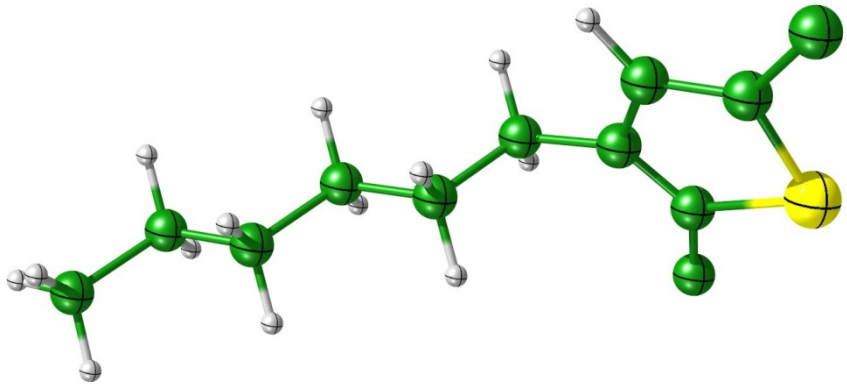

**Figure 9.** Chemical structure of poly (3-hexylthiophene) P3HT.

The optical bandgap of P3HT is about 1.9 eV that approaches the spectral peak of 1.8 eV (700 nm) of solar light corresponding to terrestrial illumination conditions of AM1.5. P3HT also has high absorption coefficient permitting efficient processing of light with wavelengths up to 650 nm using a film that is only 200 nm thick. The photoactive layer is composed by a heterojunction of two organic semiconductors. Illumination generates excitons that become separated at the junction, producing carrier flow that is collected at the contacts (Fig. 10).

One of the ways to increase current output of the cell is to improve light absorption in the photoactive layer, which can be achieved by reducing the band gap of the polymer. The conjugated polymers, characterized by a high value of absorption coefficient ($10^5$ $cm^{-1}$) look as promising candidates in this regard. While the crystalline silicon cells should be approximately 100 μm thick for efficient absorption of the incident light, organic semiconductors with direct bandgap will have the similar performance with reduced thickness of 100-500 nm. However, conjugated polymers are usually characterized with large gap values that are not always sufficient for efficient absorption.

http://dx.doi.org/10.5772/54058

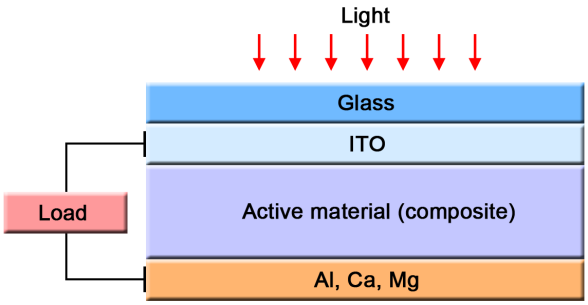


**Figure 10.** Photovoltaic solar cell: organic material sandwiched between two electrodes. The electrons are collected at the rear metal contact and the holes – at the front ITO contact.

In most organic semiconductors, excitons are comparatively tightly bound and do not dissociate easily. That is why it is useful to create a heterojunction of materials with distinct electron affinities and ionization energies to favor exciton dissociation. In this way, the electron is accepted by the material with higher affinity and the holes proceed to the material with lower ionization energy, producing the effect of a local field separating carriers at the junction. When the donor molecule is excited, an electron is transferred from HOMO to lowest unoccupied molecular orbital (LUMO), forming a hole. If electron-hole pair recombines, luminescence is produced. However, if the LUMO of the acceptor is small enough compared to that of the donor, the excited electron will end up at acceptor's LUMO and the carriers originating from dissociated exciton will be separated (Figure 11).

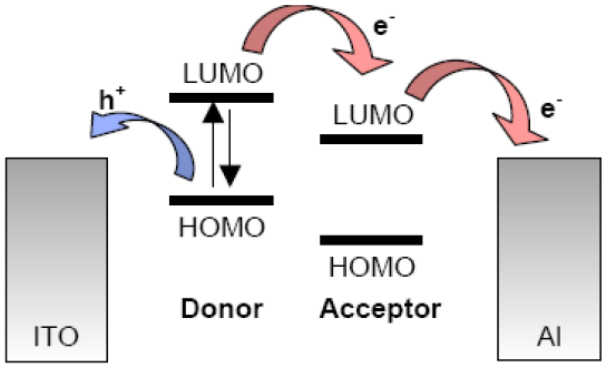


**Figure 11.** Exciton dissociation at the donor-acceptor interface

The heterojunction cells will be efficient in dissociation of excitons at the interface area [29], requiring generation of an exciton within its diffusion length from the interface. As diffusion length value is about 10 nm, it limits the thickness of light-absorbing layer. On the other hand, for the majority of organic semiconductors it is necessary to have a film of more than

100 nm thick to ensure sufficient light absorption, which, in turn, lowers the number of excitons that can reach the interface. For this reason, it is proposed to obtain dispersed (bulk) heterojunctions, schematically depicted in Fig 12.

One of the main problems to create such type of solar cells concerns miscibility of the components. Conjugated systems – including polymer conjugates and dyes – are usually immiscible, so that even a completed solar cell may represent a non-equilibrium system. To improve the situation somehow, it is proposed to use the spin coating technique that is characterized with rapid solvent evaporation, requires little parameter adjustments and tolerates a wide range of viscosities. The deposition process usually has three steps: dispersion of nanoparticles in a solvent, mixing them with a polymer and finally molding of the compound. Other techniques, such as co-evaporation and co-sputtering allow better control over morphology of the material; however, they are quite costly due to particular temperature and pressure requirements (e.g., deposition should be carried out in vacuum).

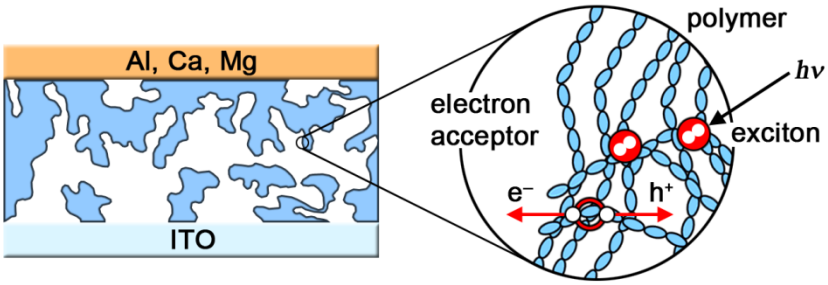


**Figure 12.** Architecture of a photovoltaic cell with a dispersed heterojunction formed by conjugated polymer with transparent ITO front electrode and Al, Ca, Mg rear electrode.

A new generation of solar cells called hybrid polymer solar cells attracts a considerable interest [30-31]. Recent studies have shown that nanoparticles incorporated into photoactive layer improve light absorption and increase photocurrent. Nanoparticle polymer-based photovoltaic cells have a long term potential for decreasing the cost and improve device efficiency. The maximum efficiency reported to date is around 5.55% (with theoretical predictions of about 10%). Incorporation of 5-10 nm nanoparticles of gold into poly (9.9-dioctylfluorene) results in significant improvement of cell efficiency and oxidation stability.

## 6. Heating issues and their treatment

Direct absorption of energy from the sunlight faces another considerable problem connected with operation of electronic devices under elevated temperatures due to variation of band gap of semiconductors, increase of thermal noise, etc. A partial solution to this problem can be offered by the use of passive/active radiators that will dissipate some of excessive heat. Further development of this idea leads to the use of hybrid systems that allow to process

http://dx.doi.org/10.5772/54058

part of solar light via photoelectric conversion, storing thermal energy, for example, by heating water that can be used for household needs. This, however, does not allow to reduce the problems of high-temperature operation of an electronic device (solar cell) considerably. A useful solution can be glimpsed from the nanoelectronics, which also have problems with removal of excess heat from the integrated circuits. Thermal management in these devices has become problematic because faster and denser circuits are required to meet the modern needs, which, in turn, produces even more heat. Localized areas of high heat flux influences the performance at both the chip and the board levels for the current nanotechnologies.

Key concepts like waste heat recycling or waste heat recovery are the basic ideas in the design of the newest heat protection and dissipation systems. The potential applications of the thermoelectric devices are thus enormous. Thermoelectricity is the revolutionary technology that is currently under intense development aiming to find a solution to thermal management problem and protection of small-scale systems. However, due to relatively low efficiency (around 10%), thermoelectric cooling is generally only used in small systems; the new concepts based on nanoscale heat transfer bring a new opportunity to widen the application horizons for thermoelectric devices.

As expected, technology scaling significantly impacts power dissipation issues. The scale-connected effects for silicon-on-insulator (SOI) technology affect electrical properties of the material. Joule heat generated in SOI transistors may compromise long term reliability of the device. The thermal conductivity of the channel region of nanometer transistors is significantly reduced by phonon confinement and boundary scattering. This increases the thermal resistance of the device, leading to higher operating temperatures compared to the bulk transistors of the same power input. However, ballistic transport between the material boundaries impedes device cooling, so that temperature-dependent parameters of the device such as source-drain current and threshold-current will increase significantly, generating much Joule heat that will eventually lead to accelerated temperature degradation of the gate dielectric [32, 33]. The recently developed germanium-on-insulator (GeOI) technology combines high carrier mobility with the advantages of the SOI structure, offering an attractive integration platform for the future CMOS devices [34].

SiGe nanostructures are very promising for thermoelectric cooling of microelectronic devices and high-temperature thermoelectric power generation. It has been demonstrated that the thermal conductivity is significantly reduced in super-lattices [35-37] and quantum dot super-lattices [38-40]. A self-organized set of vertically stacked Si/Ge quantum dots is a good alternative to induce artificial scattering of phonons and reduce the thermal conductivity. One of the ways to increase scattering even more involves creation of the structure where with uncorrelated vertical positions of quantum dots, reducing the effective thermal path of the phonon within the Si layer as shown in Figure 13. The phonons travelling by the pathway laid by Ge quantum dots will experience higher scattering than phonons travelling through the Si pathway only. This effect becomes even more efficient because, in fact, the phonons spreading through Ge quantum dots will suffer a sequence of scattering events from one dot to another. As one can see from the figure, temperature-dependent cross-plane thermal conductivity reduces dramatically in Ge

quantum dot superlattices depending on vertical correlation between dots, with at least twice lower thermal conductivity value obtained for the case of uncorrelated dot structures in comparison with well-aligned dot array with the same vertical spacing of 20 nm. The same result can be confirmed by Raman spectroscopy [41].

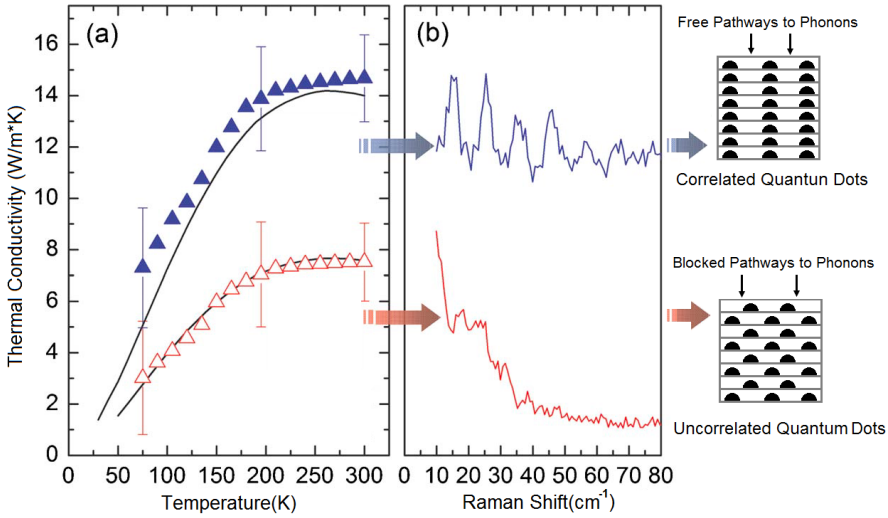


**Figure 13.** Dependence of thermal conductivity on the temperature for correlated and uncorrelated Ge quantum dot structures

Thin film single-crystalline GeOI structures may be considered as potential candidates in the field of CMOS microelectronics improving thermal performance of transistors due to superior mobility of carriers compared to other semiconductors. Recent predictions in the thermal conductivity of ultra-thin germanium films suggest that the small bulk mean free path of Ge will induce a weaker effect on the boundary scattering [42]. This thermal behavior is an additional reason that makes GeOI structures competitive with SOI for the case of small-size thin film devices at the cutting edge of the technology. For example, it has been reported from Monte Carlo modeling that electro-thermally optimized GeOI structures should be 30% more productive than the best SOI device examples [34]. In addition, the higher mobility of germanium implies that GeOI devices might support the same amount of current at lower operating voltage, so that the dissipated power is expected to be lower [42].

Figure 14 shows a plot of the intrinsic out-of-plane thermal conductivity variation with thickness at 300 K. In spite of low thermal conductivity of bulk Ge compared to that of Si ($\kappa_{Ge}/\kappa_{Si}$ ~ 0.4), ultra-thin films of germanium has smaller thermal conductivity due to reduced mean free path. Hence, ultra-thin films of Ge suffer from a lower reduction of the thermal conductivity compared to ultra-thin films of Si, which makes germanium-on-insulator structures promising candidates for devices with reduced self-heating effects compared to silicon-on-insulator structures [43].

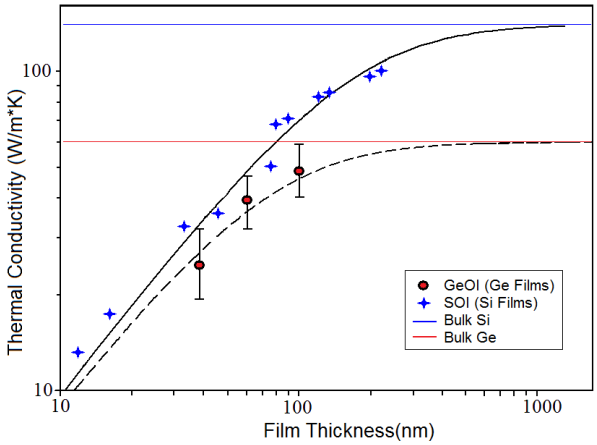


**Figure 14.** Dependence of thermal conductivity $\kappa$ on film thickness for different materials.

The experience obtained with aforementioned thermoelectric applications can be successfully applied to the field of photovoltaics, forming efficient heat-draining layers either on the frontal surface of solar cells that suffer highest temperature increase or over the contact grid that, in addition to solar heating, also experiments Joule heat.

## 7. Conclusions

This chapter addresses a wide number of topics concerning thin-film solar cells. It was shown that the numerical modeling of current transport in AlGaAs/GaAs heterojunctions allows to determine optimal aluminum content (that defines band gap difference of the junction components) ensuring the most efficient processing of the incident light flux by window and absorber layers. We found that for very thin window layers the proximity of the junction area to the surface of the cell has more prominent role, allowing the embedded field of space charge region to function more intensively in separation of photo-generated currents and reducing the effect of recombination phenomena.

The question concerning quality improvement of junction boundary is reflected in the second section that presents results concerning the use of isovalent substitution method for manufacturing of heterojunction solar cells. As substituted layers grow into the substrate, we obtain a smooth transition of one material into another that reduces the difference of lattice constants and thermal expansion coefficients, both of which are of high importance for photovoltaic devices. Good efficiency values for non-optimized cells without any special anti-reflection coatings and with considerable series resistance paves the way for future improvements.

A special attention is being paid to creation of cheap and environment-friendly technologies for solar cells; this point is illustrated with an example of CdS/PbS heterojunctions created

by ammonia-free chemical bath deposition. It is thought that these results will be interesting for large-scale industrial production of solar cells.

We address the important questions of organic solar cells, which nowadays attract much attention of the scientific community. These photovoltaic devices has lower efficiency in comparison with silicon or tandem multi-junction cells, but they are incomparably cheaper and can use flexible substrates, which opens completely new and wide horizons for their possible applications. We also discuss the problems of the proper choice of organic material for the active element of the cell.

Finally, solar cells are always overheated due to exposure to a direct sunlight, which makes a considerable problem concerning degradation of device parameters under prolonged operation under elevated temperatures, as well as mechanical stability of the cell due to thermal expansion of its components. We propose to make some useful parallels with nanoelectronics, which recently received promising solutions in a form of thermoelectric heat transfer managing devices. We hope that the similar techniques could be applied to solar cells, offering good results with temperature control for photovoltaics, especially those operating under concentrated sunlight conditions.

## Author details

P.P. Horley[1], L. Licea Jiménez[1,2], S.A. Pérez García[1,2], J. Álvarez Quintana[1,2], Yu.V. Vorobiev[3], R. Ramírez Bon[3], V.P. Makhniy[4] and J. González Hernández[1]

1 Centro de Investigación en Materiales Avanzados, Chihuahua - Monterrey, México

2 GENES Group of Embedded Nanomaterials for Energy Scavenging, Apodaca, México

3 Centro de Investigación y Estudios Avanzados Unidad Querétaro, Querétaro, México

4 Yuri Fedkovych Chernivtsi National University, Chernivtsi, Ukraine

## References

[1] Green MA. Silicon Solar Cells: Advanced Principles and Practice. Sydney: Bridge; 1995.

[2] Gonçalves da Silva C. The Fossil Energy/Climate Change Crunch: Can we Pin our Hopes on New Energy Technologies?, Energy 2010; 35 1312–1316.

[3] Green MA, Emery K, Hishikawa Y, Warta W, Dunlop ED. Solar Cells Efficiency Tables (Version 38), Progress in Photovoltaics: Research and Applications 2011; 19 565-572.

[4] Hillhouse HW, Beard MC. Solar Cells from Colloidal Nanocrystals: Fundamentals, Materials, Devices, and Economics. Current Opinion in Colloid & Interface Science 2009; 14 245–259.

[5] Chopra K, Das A. Thin Film Solar Cells. New York: Plenum Press, 1986.

[6] Farhenbruch A, Bube R. Fundamentals of Solar cells. New York: Academic Press, 1983.

[7] Pauwels HJ, De Visschere P, Reussens P. Analysis of Generation in Space Charge Regions of Solar Cells. Solid State Electronics 1978; 21 775-779.

[8] Serdyuk VV. Physics of Solar Elements. Odessa: Logos, 1994.

[9] Hovel HJ, Woodwall JM. $Ga_{1-x}Al_xAs$-GaAs p-n Heterojunction Solar Cells. Journal of Electrochemical Society 1973; 120 1246.

[10] Hulstorm R, Bird R, Riodan C. Spectral Solar Irradiance Data Sets for Selected Terrestrial Conditions. Solar Cells 1985; 15 365.

[11] Ponpon JP. A Review of Ohmic and Rectifying Contacts on Cadmium Telluride. Solid State Electronics 1985; 28(7) 689-706.

[12] Sharma BL, Purohit RK. Semiconductor Heterojunctions. NY: Pergamon Press, 1974.

[13] Makhiny VP, Baranyuk VE, Demich NV, et al. Isovalent Substitution: a Perspective Method of Producing Heterojunction Optoelectronic Devices. Proc. SPIE 2000; 4425 272.

[14] Ryzhikov VD. Scintillation Crystals of $A^2B^6$ Semiconductors. Moscow: NIITEHIM, 1989.

[15] Nakada T, Mitzutani M, Hagiwara Y, Kunioka A. High-efficiency Cu(In,Ga)Se2 Thin Film Solar Cells with a CBD-ZnS Buffer Layer, Solar Energy Materials and Solar Cells 2001; 67 255–260.

[16] De Melo O, Hernandez L, Zelaya-Angel O, Lozada-Morales R, Becerril M, Vasco E. Low Resistivity Cubic Phase CdS Films by Chemical Bath Deposition Technique, Applied Physics Letters 1994; 65 1278–1281.

[17] Ortuño-López MB, Valenzula-Jauregui JJ, Sotelo-Lerma M, Mendoza-Galvan A, Ramírez-Bon R. Highly Oriented CdS Films Deposited by an Ammonia-Free Chemical Bath Method. Thin Solid Films 2003; 429 34–39.

[18] Hernández-Borja J, Vorobiev YV, Ramírez-Bon R. Thin Film Solar Cells of CdS/PbS Chemically Deposited by an Ammonia-Free Process. Solar Energy Materials & Solar Cells 2011; 95 1882–1888.

[19] Green MA. Third Generation Photovoltaics: Ultra-High Efficiency at Low Cost. Berlin: Springer-Verlag, 2003.

[20] Krebs FC. Fabrication and Processing of Polymer Solar Cells: a Review of Printing and Coating Techniques. Solar Energy Materials and Solar Cells 2009; 93 394–412.

[21] Zhou QM, Hou Q, Zheng L et al. Fluorene-based Low Band-gap Copolymers for High Performance Photovoltaic Devices. Applied Physics Letters 2004; 84 1653–1655.

[22] Xin H., Ren G., Sunjoo Kim F., Jenekhe SA. Bulk Heterojunction Solar Cells from Poly(3-butylthiophene)/ Fullerene Blends. Chemical Materials 2008; 20 6199–6207.

[23] Wang G, Swensen J, Moses D, Heeger AJ. Increased Mobility from Regioregular Poly(3-hexylthophene) Field-Effect Transistors. Journal of Applied Physics 2003; 93(10) 6137.

[24] Hebner TR, Wu CC, Marcy D, Lu MH, Sturm JC. Ink-jet Printing of Doped Polymers for Organic Light Emitting Devices. Applied Physics Letters 1998; 72(5) 519.

[25] Chang SC, Liu J, Bharathan J, Yang Y, Onohara J, Kido J. Mutlicolor Organic Light-Emitting Diodes Processed by Hybrid Inkjet Printing. Advanced Materials 1999; 11 734.

[26] Pschenitzka F, Sturm JC. Three-color Organic Light-emitting Diodes Patterned by Masked Dye Diffusion. Applied Physics Letters 1999; 74(13) 1913.

[27] Rogers JA, Bao Z, Raju VR. Nonphotolithographic Fabrication of Organic Transistors with Micron Feature Sizes. Applied Physics Letters 1998; 72(21) 2716.

[28] Gustafsson G, Cao Y, Treacy GM, Klavetter F, Colaneri N, Heeger AJ. Flexible Light-Emitting Diodes Made from Soluble Conducting Polymers. Nature 1992; 357 477-478.

[29] Saunders BR, Turner ML. Nanoparticle–Polymer Photovoltaic Cells. Advances in Colloid and Interface Science 2008; 138 1–23.

[30] Sariciftci NS, Smilowitz L, Heeger AJ, Wudl F. Photoinduced Electron Transfer from a Conducting Polymer to Buckminsterfullerene. Science 1992; 258 1474-1476.

[31] Yu G, Gao J, Hummelen JC, Wudl F, Heeger AJ. Polymer Photovoltaic Cells: Enhanced Efficiencies via a Network of Internal Donor-Acceptor Heterojunctions, Science 1995; 270 1789-1791.

[32] Fiegna C, Yang Y, Sangiorgi E, O'Neill AG. Analysis of Self-Heating Effects in Ultrathin-Body SOI MOSFETs by Device Simulation. IEEE Transactions on Electron Devices 2008; 55(1) 233-244.

[33] Pop E, Sinha S, Goodson KE. Heat Generation and Transport in Nanometer-Scale Transistors. Proccedings of the IEEE 2006; 94 (8) 1587-1601.

[34] Lee ML, Fitgerald EA. Strained Si/Strained Ge Dual-Channel Heterostructures on Relaxed $Si_{0.5}Ge_{0.5}$ for Symmetric Mobility p-type and n-type Metal-Oxide-Semiconductor Field-Effect Transistors. Applied Physics Letters 2003; 83(20) 4202.

[35] Lee SM, Cahill DG, Venkatasubramanian R. Thermal Conductivity of Si-Ge Superlattices. Applied Physics Letters 1997; 70 2957.

[36] Lu X, Chu J. Lattice Thermal Conductivity in a Si/Ge/Si Heterostructure. Journal of Applied Physics 2007; 101 114323.

[37] Kiselev AA, Kim KW, Stroscio MA. Thermal Conductivity of Si/Ge Superlattices: A Realistic Model with a Diatomic Unit Cell. Physical Review B 2000; 62 6896.

[38] Liu JL, Khitun A, Wang KL, et al. Cross-Plane Thermal Conductivity of Self-Assembled Ge Quantum Dot Superlattices. Physical Review B 2003; 67 165333.

[39] Shamsa M, Liu W, Balandin A, Liu J. Phonon-Hopping Thermal Conduction in Quantum Dot Superlattices. Applied Physics Letters 2005; 87 202105.

[40] Lee LL, Venkatasubramanian R. Effect of Nanodot Areal Density and Period on Thermal Conductivity in SiGe/Si Nanodot Superlattices. Appl. Phys. Lett. 2008; 92 053112.

[41] Alvarez-Quintana J, Alvarez X, Rodriguez-Viejo J, Jou D, Lacharmoise PD, Bernardi A, Goñi AR, Alonso MI. Cross-plane Thermal Conductivity Reduction of Vertically Uncorrelated Ge/Si Quantum Dot Superlattices. Applied Physics Letters 2008; 93 013112.

[42] Pop E, Chu CO, Dutton R, Sinha S, Goodson K. Electro-Thermal Comparison and Performance Optimization of Thin-Body SOI and GOI MOSFETs. IEDM Technical Digest. IEEE International 2004; 411-414.

[43] Alvarez-Quintana J, Rodríguez-Viejo J, Alvarez FX, Jou D. Thermal Conductivity of Thin Signle-Crystalline Germanium-on-Insulator Structures. International Journal of Heat and Mass Transfer 2011; 54 1959–1962.